


Direct characterization of shear phonons in layered materials by mechano-Raman spectroscopy

Received: 8 September 2022

Accepted: 23 February 2023

Published online: 30 March 2023


 Check for updates

Susu Fang ^{1,9}, Sai Duan ^{2,9}, Xingzhi Wang³, Sijie Chen ⁴, Li Li ¹, Hua Li¹, Baichuan Jiang ¹, Chuanhui Liu ¹, Nanyang Wang ⁵, Lei Zhang ¹, Xinglin Wen ⁴, Yagang Yao ⁵, Jun Zhang ⁶, Daiqian Xie ^{1,7}  & Weigao Xu ¹ 

Shear phonons are collective atomic-layer motions in layered materials that carry critical information about mechanical, thermal and optoelectronic properties. Phonon branches with co-directional atomic-layer motions carry unique information about the global structure and hidden interfaces in layered crystals and heterostructures, but they are not detectable due to the very limited electron–phonon coupling. Here we utilize the propagating feature and mechanical coupling between shear phonons and localized plasmonic cavities to successfully realize direct characterization of ground-state shear phonons down to 4 cm^{-1} in energy by introducing mechano-Raman spectroscopy (MRS). MRS has the ability to characterize the global crystal structure with more than 10^3 -fold enhancement and to accurately measure subpicometre displacements under ambient conditions with a thermal-noise-free feature. The propagating behaviour and the capacity of MRS to detect optically hidden interfaces are demonstrated. The broad tunability of plasmons makes the MRS technique a robust tool for extensive applications, including global crystal flaw detection, mechanical sensing and the mechanical modulation of light.

Van der Waals layered systems give rise to previously inaccessible and interesting physical properties^{1–7} via the tailoring of interlayer interactions. Such interactions are mysterious and hard to fully decipher⁸, although substantial progress has been made through the use

of optical^{2,9}, electrical⁴, magnetic⁵ and thermal⁷ approaches. Among all the types of interlayer interaction, mechanical interactions have a dominant role because they directly correlate with the atom-level interfacial structure and functionality. Besides offering rich information on

¹Key Laboratory of Mesoscopic Chemistry, School of Chemistry and Chemical Engineering, Nanjing University, Nanjing, China. ²Collaborative Innovation Center of Chemistry for Energy Materials, Shanghai Key Laboratory of Molecular Catalysis and Innovative Materials, MOE Key Laboratory of Computational Physical Sciences, Department of Chemistry, Fudan University, Shanghai, China. ³Department of Physics, Xiamen University, Xiamen, China. ⁴School of Optical and Electronic Information, Wuhan National Laboratory for Optoelectronics, Huazhong University of Science and Technology, Wuhan, China. ⁵National Laboratory of Solid State Microstructures, College of Engineering and Applied Sciences, Jiangsu Key Laboratory of Artificial Functional Materials and Collaborative Innovation Center of Advanced Microstructures, Nanjing University, Nanjing, China. ⁶State Key Laboratory for Superlattices and Microstructures, Institute of Semiconductors, Chinese Academy of Sciences, Beijing, China. ⁷Hefei National Laboratory, Hefei, China. ⁸Hefei National Research Center for Physical Science at the Microscale and Synergetic Innovation Center of Quantum Information & Quantum Physics, University of Science and Technology of China, Hefei, China. ⁹These authors contributed equally: Susu Fang, Sai Duan.  e-mail: dqxie@nju.edu.cn; yiluo@ustc.edu.cn; xuwg@nju.edu.cn

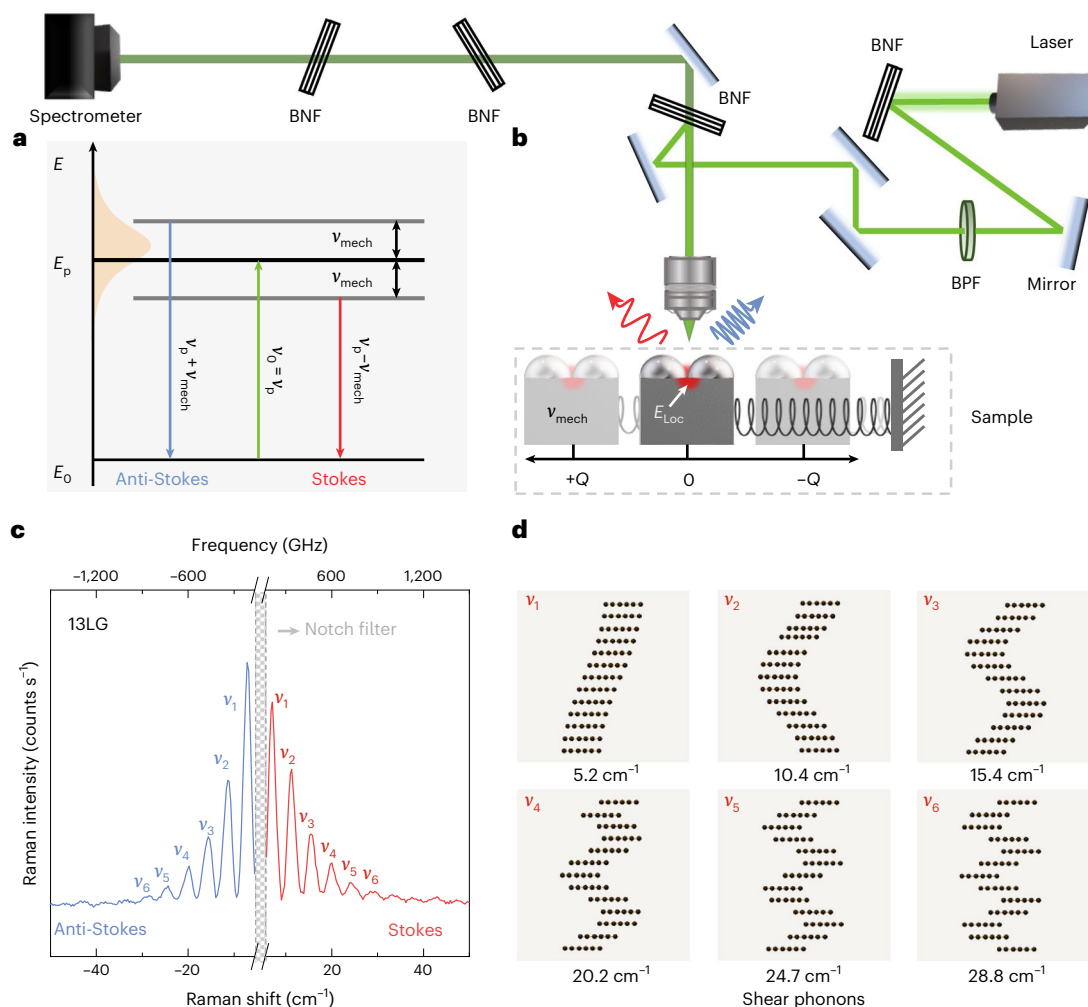


Fig. 1 | MRS for direct frequency-domain detection of mechanical vibrations.

a, Energy diagram of a mechano-Raman scattering process. ν_p and ν_0 are the frequencies (in cm^{-1}) of resonantly excited surface plasmons and incident photons, respectively. We have $\nu_p = \nu_0$. E_0 and E_p are the energy levels of the ground-state and excited-state electrons in the plasmonic metal. The schematic illustrates the coupling between the plasmonic cavity and a vibrator (mechanical vibrator frequency, ν_{mech}). **b**, Schematics of the experimental set-up for MRS.

A mechanical vibrator exerts a periodic force on the plasmonic metal, and the periodic polarizability change of the plasmonic cavity causes the inelastic Raman scattering (one-dimensional displacement, $\pm Q$). BPF, bandpass filter; BNF, BraggGrate notch filter. **c**, MRS spectrum of a 13LG. Excitation is provided by a 532-nm laser (9.43 mW, 150 s). The shaded area marks the part blocked by the notch filter. **d**, Atomic-layer motions of ν_1 to ν_6 of a 13LG.

electron–phonon coupling^{10–12} and heat transport¹³, interlayer phonons are the most straightforward and informational medium for providing details on mechanical coupling and propagation, making them vital to the design and development of next-generation, intelligent van der Waals materials.

Optical Raman spectroscopy has been widely used as a tool for phonon detection based on a direct light–vibrator inelastic scattering process¹⁴. In the past, the experimental measurement of shear phonons has been restricted by the limited electron–phonon interaction strength¹⁰. If we take 16-layer graphite (16LG) as an example, only the highest-frequency interlayer shear phonon (42 cm^{-1}) is optically detectable¹⁰, because the relative intensities of the lowest and second-lowest ones, as estimated by theory, are -9.1×10^{-7} and 0, respectively. The propagating characteristics of such lower-frequency phonons carry information about the global structure and hidden interfaces; however, none of the well-established techniques is as yet capable of tracing them experimentally.

The investigation of optically dark processes usually brings a revolutionary understanding and knowledge of the functionalities of matter^{15,16}. To capture mechanical information from the interlayer interactions, it is necessary to build a bridge between mechanical

vibrators and spectroscopic technologies. Over the years, several pioneering theoretical and experimental attempts have been made that take advantage of optomechanical effects by placing molecule vibrators inside a plasmonic cavity^{17–20}. With this in mind, in this Article we propose a feasible and more general approach that mechanically couples phonon vibrators with plasmons. In this scenario, each phonon vibrator periodically drives the plasmonic nanostructures through collected mechanical motions from the atomic layers, resulting in specific mechanical modulation of the plasmonic frequency and intensity that is directly detectable in energy space. The use of plasmons as the scattering medium has at least three advantages: a large scattering section with incident light^{21–26}, easy coupling with the vibrator^{17–19} and high compatibility with different excitation wavelengths^{27,28}. It should be emphasized here that other quasiparticles with non-zero dipole polarization can also, in principle, act as the scattering medium to achieve the required mechanical couplings.

The concept of mechanical coupling between plasmons and a mechanical vibrator is illustrated in Fig. 1a. Incident light (ν_0) creates a synchronous oscillating dipole in the plasmonic metal nanostructure under resonant excitation. The induced electric-dipole vector of the plasmonic cavity can be expressed as $\chi_0 E_{\text{Loc},0}(\mathbf{r}) \cos(\nu_p t)$, where χ_0 is

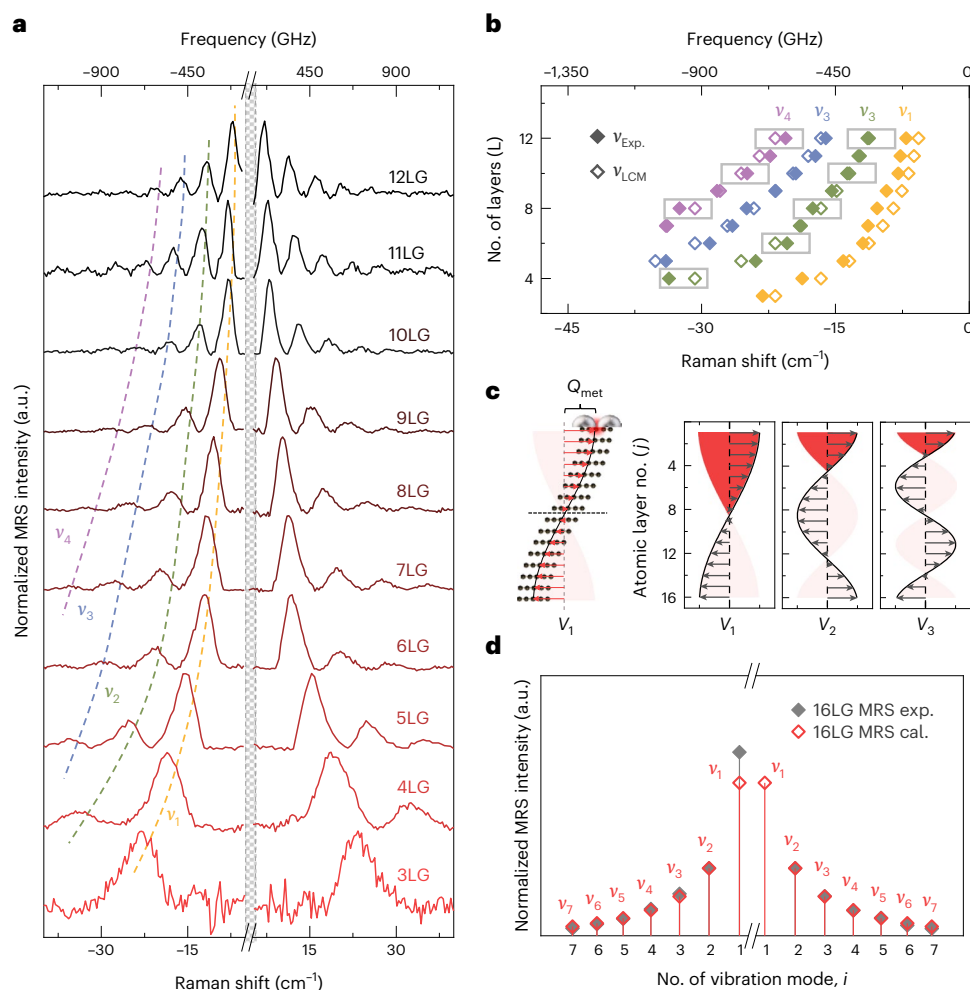


Fig. 2 | MRS for dark phonon observation and quantitative mechanical investigations. **a**, MRS spectra of N -layer graphite. **b**, Peak positions for N -layer graphite as extracted in **a** (filled symbols), as well as the corresponding LCM calculation results (open symbols). Grey boxes mark optically dark vibrations whose tensors of polarizability are zero. **c, d**, Quantitative investigation of the MRS intensity for shear phonon vibrators with different vibration mode number

i. Atomic displacements (left) and phonon wavefunction plots (right) for v_1 , v_2 and v_3 (**c**), where the y axis represents the atomic layer number (j), and V_{ij} is the displacement vector of the j th atomic layer for i th vibration mode. The dashed line marks the nodal plane. In **d**, the experimental intensity profile (filled symbols) for v_i ($i = 1-7$) has good consistency with the MRS model (open symbols), according to the equation $I_{\text{MRS, shear mode}} \propto p_i^2 \sum_j V_{i,j}^2 \left| \int \mathbf{E}_{\text{Loc},0}(\mathbf{r}) d\mathbf{r} \right|^2$.

the intrinsic polarizability of the plasmonic cavity, and $\mathbf{E}_{\text{Loc},0}(\mathbf{r})$ and v_p are the spatial distribution of the amplitude of the plasmonic field vector and the frequency of the localized incident light, respectively. Here we take advantage of the non-propagating feature of the localized plasmonic field; once remote coupling occurs, the localized plasmon will be modulated by a mechanical vibrator with frequency v_{mech} . Retaining the first-order approximation, the dipole moment induced by the mechanical vibrator can be described by classical mechanics as $\frac{1}{2} \left| \frac{\partial \chi}{\partial Q_{\text{met,tot}}} \right| Q_{\text{met,tot}} \mathbf{E}_{\text{Loc},0}(\mathbf{r}) \cos[(v_p \pm v_{\text{mech}})t]$ where $\frac{\partial \chi}{\partial Q_{\text{met,tot}}}$ is the first derivative of the polarization tensor, and $Q_{\text{met,tot}}$ is the displacement vector of the plasmonic metal under mechanical modulation (Supplementary Section 2 and Supplementary equation 6). Finally, there is a remote energy transfer between the mechanical vibrator and the resonant plasmon, resulting in a Stokes Raman ($v_0 - v_{\text{mech}}$) and an anti-Stokes Raman ($v_0 + v_{\text{mech}}$) signal. We call this new type of spectroscopic technology ‘mechano-Raman spectroscopy’ (MRS).

The implementation of an MRS experiment requires a characterized system and a suitable investigating object. The optical set-up and sample configuration for MRS are presented in Fig. 1b. We used multiple BraggGrate notch filters (BNFs) to purify the excitation laser and block the excitation light when collecting the ultralow-frequency

scattering signal. In shear phonons, all the atoms in each individual layer are treated as one rigid ball and share the same displacement vector, and each layer moves differently to form lattice waves with different characteristic frequencies. Lower-frequency phonons, in particular, will cause net displacements in the horizontal direction (Supplementary Fig. 1). This guarantees an effective energy transfer with electronic oscillations under a back-scattering set-up. As illustrated more intuitively in Supplementary Video 1, such phonons are indeed ideal vibrators to drive the plasmonic metal.

We conducted an MRS experiment for 13-layer graphite (13LG) after placing on Ag nanoislands on the 13LG. Strikingly, a series of prominent and narrow Raman features are seen, located symmetrically on both sides of the Rayleigh scattering line (Fig. 1c). These are invisible in optical Raman spectroscopy (Supplementary Fig. 2). Notably, these emergent signals are exactly the Stokes and anti-Stokes MRS signals, which agree well with the theoretical frequencies of shear phonons¹⁰. In layered materials, according to the linear chain model (LCM)¹⁰, an N -layer graphite piece has $(N - 1)$ degenerate types of shear mode (Supplementary Table 1). Here, the v_i mode is defined as the i th shear mode in an N -layer sample starting from the lowest frequency. Figure 1d displays the atomic-layer motions of v_1 to v_6 in a 13LG, corresponding to Fig. 1c. To ensure that the emergent signals are from MRS,

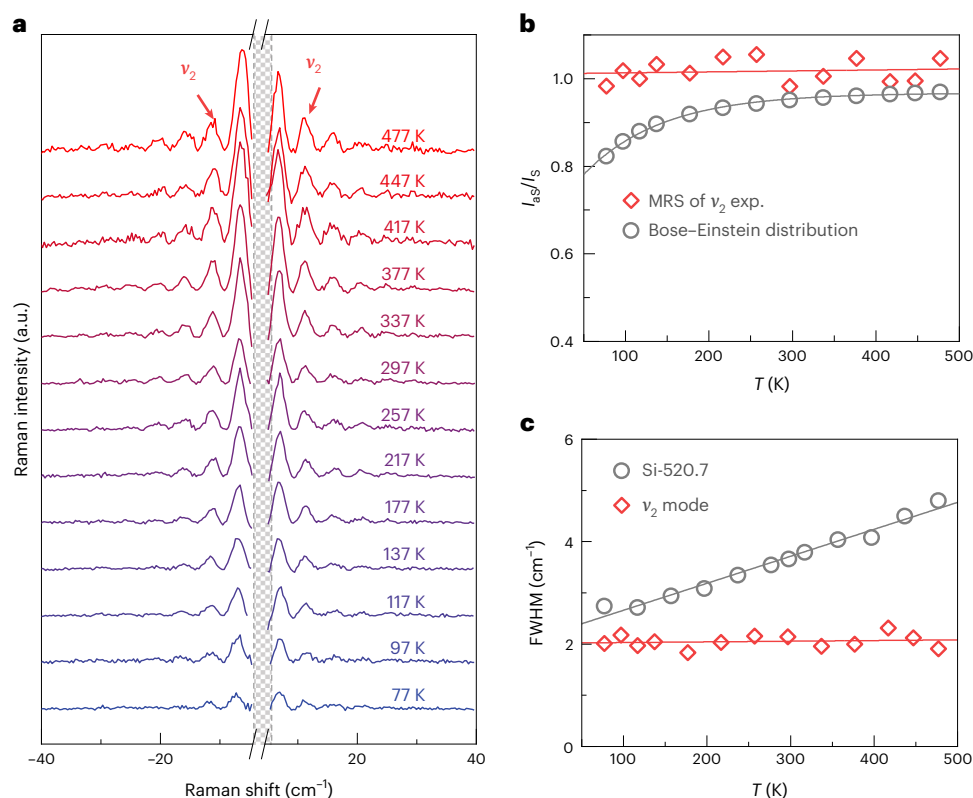


Fig. 3 | Thermal-noise-free feature of MRS. a, The in situ temperature-dependent MRS spectra of 13LG. The temperature range is 77–477 K. **b**, Temperature dependence of the integrated anti-Stokes and Stokes intensity ratio (I_{as}/I_s) of the ν_2 mode. Experimental MRS values and the calculated Bose–

Einstein distribution values are plotted in red and grey, respectively. **c**, Temperature dependence of the FWHM of the ν_2 mode (red). The first-order phonon of Si (520.7 cm⁻¹) is also plotted as a reference (grey).

possible disturbances from electromagnetic-field enhancement²⁹ were excluded (detailed discussions are provided in Supplementary Sections 2 and 3 and Supplementary Fig. 3).

MRS can be conveniently exploited to identify shear vibrators with different numbers of layers. Figure 2a presents MRS investigations of a series of AB-stacked graphite flakes (from three layers (3L) to 12 layers (12L)). The experimental vibrational frequencies of all emergent signals match the LCM-calculated results well (Fig. 2b and Supplementary Table 1), and it is worth emphasizing that all these signals are invisible in optical Raman spectroscopy. The grey boxes in Fig. 2b mark the inactive Raman modes with zero polarizability. Remarkably, MRS is sensitive enough to detect phonon-driven motions from the plasmonic metal down to 3LG, where unambiguous MRS signals occur at ± 23.1 cm⁻¹. We have also successfully utilized MRS to characterize many other layered materials, including semiconductors (for example, MoS₂ and WSe₂) and insulators (for example, hexagonal boron nitride (h-BN)), as shown in Supplementary Fig. 4. The above results indicate that MRS is an ingenious and versatile way of studying mechanical features that are otherwise inaccessible. We have examined the role of resonant excitation of the plasmon medium and performed MRS analyses with different excitation wavelengths (Supplementary Fig. 5). Given that the plasmonic medium is tunable in a broad wavelength range from the ultraviolet to infrared regions³⁰, we anticipate that the MRS technique is suitable for on-demand analysis in various application scenarios.

We also demonstrated the capacity of MRS for quantitative measurement of a tiny amount of vibration amplitude. Based on the mechanical coupling nature between plasmons and the vibrator, the Raman intensity of each mode was determined by the polarizability tensor of the plasmonic cavity, which is dynamically modulated by each shear phonon. The polarization tensor is directly related to the displacement

vector of the plasmonic metal, $Q_{\text{met,tot}}$. Generally, $Q_{\text{met,tot}} = Q_{\text{met,0}} + pQ_{\text{mech}}$, where p is the plasmon–vibrator mechanical coupling efficiency and $Q_{\text{met,0}}$ is the eigen displacement vector of the plasmonic metal. We have $Q_{\text{met,0}} = 0$, considering the zero net displacements of the plasmonic metal without an external driver. For a perfectly coupled system in which the motions between vibrator and plasmon are fully synchronized, we have $p = 1$, and thus $Q_{\text{met,tot}} = Q_{\text{mech}}$. For an uncoupled system, the plasmon is regarded as an eigenstate ($p = 0$). Integral of all space, the perturbation term would result in a radiative dipole. In other words, the intensity is proportional to $\left| \frac{\partial \chi}{\partial Q_{\text{met,tot}}} \right|^2 p^2 Q_{\text{mech}}^2 \left| \int \mathbf{E}_{\text{Loc,0}}(\mathbf{r}) \mathbf{dr} \right|^2$ at a resonant energy of $\nu_{\text{MRS}} = \nu_p \pm \nu_{\text{mech}}$ in MRS. Detailed discussions are provided in Supplementary Section 2.

Taking 16LG as an example, we made a more precise analysis of the MRS process. A transmission curve of white light (after passing through BNFs) was used to calibrate the measured intensities of dark phonons (Supplementary Fig. 6). Because the frequencies of the vibrators are close to each other, the resonance-induced intensity difference was estimated to be less than 1% and thus is neglected here for calculation of the MRS intensity (Supplementary Fig. 7). According to $I \propto \left| \frac{\partial \chi}{\partial Q_{\text{met,tot}}} \right|^2 p^2 Q_{\text{mech}}^2 \left| \int \mathbf{E}_{\text{Loc,0}}(\mathbf{r}) \mathbf{dr} \right|^2$ and the degenerate nature of all shear phonon vibrators, the relative intensity of each shear vibrator in the 16LG is only determined by coupling coefficient p . As shown in Fig. 2c, the atomic movements ($V_{i,j}$) of the ν_1 mode and its phonon wavefunction are illustrated. The effective plasmon–vibrator coupling region should relate to atomic-layer motions before the first nodal plane of its phonon wavefunction, that is, the integrated regions highlighted in red in Fig. 2c. The position of the first nodal plane for the i th mode is $(N/i + 1)/2$. As a result, the

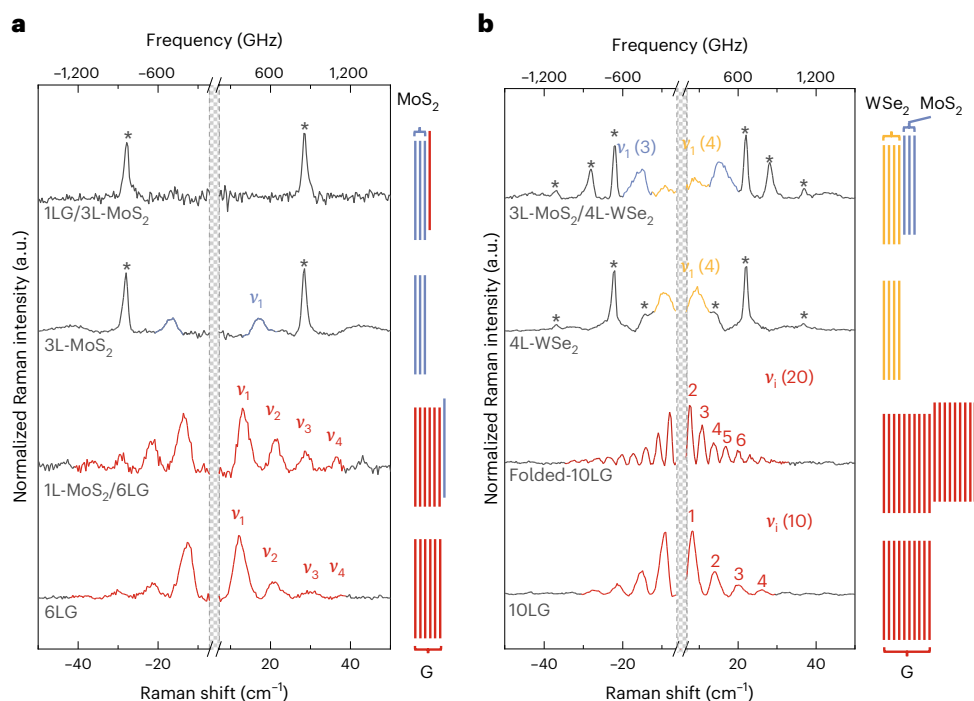


Fig. 4 | Propagating behaviour in multi-component vibrators and the capacity for hidden-interface detection. **a**, MRS of phonon vibrators covered by monolayers with different ductility, that is, 3L-MoS₂ with and without a 1LG cover layer (top) and 6LG with and without a 1L-MoS₂ cover layer (bottom), from which we can see that MRS was blocked by a ductile cover layer (1LG) and allowed by a more rigid one (MoS₂). **b**, MRS of a heterogeneous (top, 3L-MoS₂/4L-WSe₂) and a homogeneous (bottom, folded-10LG) bicomponent lattice vibrator. All

MRS signals are identified and labelled, and peaks from the optical Raman scattering process are marked with an asterisk. The schematics on the right are intended to better illustrate the sample structures. The marked MRS signals in the spectra are in accordance with the colour of the corresponding material. For clarity, all the spectra are normalized by the intensity of the strongest peak. The numbers in parentheses indicate the number of layers of a particular material.

effective energy of the vibrator, $E_{\text{eff}} \propto \int_1^{(N/i+1)/2} V_{i,j}^2 dj$, would contribute to drive the displacement of the metal ($Q_{\text{met, tot}}$). Here, the vibrator-plasmon coupling efficiency for the i th vibrator ($p_i \in [0, 1]$) can be written as $p_i = \left[\left(\int_1^{(N/i+1)/2} V_{i,j}^2 dj \right) / \left(\int_1^N V_{i,j}^2 dj \right) \right]^2$. Accordingly, we have $I_{\text{MRS, shear mode}} \propto p_i^2 \sum_j V_{i,j}^2 \left| \int \mathbf{E}_{\text{Loc},0}(\mathbf{r}) d\mathbf{r} \right|^2$. The experimental MRS intensity profile of each mode is consistent with our theoretical model (Fig. 2d). More illustrations of atomic displacements and the full set of phonon wavefunction plots are provided in Supplementary Figs. 8 and 9. As can be seen, MRS is a natural tool for the investigation of picometre-scale displacements. In the following we make a few more quantitative estimations of the capacity of MRS. As shown in Supplementary Table 2, taking the v_7 mode as an example, the equivalent displacement that drives the plasmonic metal in the v_7 mode in 16LG is -1.4 pm, and this value for $Q_{\text{met, tot}}$ will be orders of size smaller because of the much larger mass of the metal nanostructures, suggesting that MRS is an ultrasensitive tool for dynamical sensing of subpicometre displacements.

The most prominent feature of MRS is its thermal-noise-free nature, which is a rare advantage in the observation and manipulation of basic physical effects and spectroscopic applications³¹. We conducted temperature-dependent and power-dependent experiments for optical spectral vibration detection and MRS (Fig. 3 and Supplementary Fig. 10). For temperature-dependent experiments, shown in Fig. 3b, the ratio of anti-Stokes and Stokes emissions ($I_{\text{as}}/I_{\text{s}}$) for the entire temperature range of 77–477 K remains constant (~ 1). However, according to the Bose–Einstein distribution³² (that is, $I_{\text{as}}/I_{\text{s}} = \exp(-h\nu_i/k_{\text{B}}T)$), we should observe an $I_{\text{as}}/I_{\text{s}}$ value of 0.82 at 77 K for the v_2 mode (10.4 cm⁻¹). Temperature-dependent $I_{\text{as}}/I_{\text{s}}$ profiles of shear mode v_1 in a folded 2LG and first-order Si mode are also provided, and are consist-

ent with the Bose–Einstein distribution (Supplementary Fig. 11). The distinct temperature profile of $I_{\text{as}}/I_{\text{s}}$ in MRS suggests a thermal-independent excited-to-ground-state distribution. Meanwhile, on carefully analysing the full-width at half-maximum (FWHM) of the MRS signals, we found that the MRS signal of the v_2 mode of 13LG remains at -2 cm⁻¹ and shows zero thermal broadening, in stark difference to control experiments on the first-order Si mode, which broadens from 2.7 cm⁻¹ at 77 K to 4.8 cm⁻¹ at 477 K. Moreover, we noticed that the FWHM for the MRS signal v_i decreases with increasing layer thickness (Fig. 2a), which is due to a decreased damping term (Γ_{m}). Similar to a first-order Raman process, in accordance with $I \propto \left| \frac{\partial \chi}{\partial Q_{\text{met, tot}}} \right|^2 p^2 Q_{\text{mech}}^2 \left| \int \mathbf{E}_{\text{Loc},0}(\mathbf{r}) d\mathbf{r} \right|^2$, we have found a linear power-dependence of the MRS intensity, which is proportional to $\left| \int \mathbf{E}_{\text{Loc},0}(\mathbf{r}) d\mathbf{r} \right|^2$ (Supplementary Fig. 10). These distinct behaviours suggest a different mechanism of light–matter interaction between MRS and optical Raman detection, where all the characteristics in MRS are associated with the classical mechanical frame. The abovementioned features guarantee MRS as a powerful tool in various detection scenarios, with no accompanying thermal noise or spectral drift.

Phonons propagate well in materials. To further explore the interfacial propagating behaviour and the capacity for the detection of hidden interfaces, we carried out MRS investigations on a series of composite lattice vibrators, that is, layered heterostructures prepared via the aligned-transfer method². As shown in Fig. 4a, we first focus on how the ductility^{33–35} of the uppermost atomic layer affects mechano-Raman scattering generation. Interestingly, by comparing the MRS measurements of 1L-MoS₂ on 6LG and 1LG on 3L-MoS₂, we found that a more rigid structure^{36,37} (for example, 1L-MoS₂) will maintain the long-range propagation of phonon vibrations, whereas a ductile one (such as

1LG) is found to be able to buffer the shear force and hinder the MRS process³⁸. This suggests that monolayer graphene is a perfect vibration isolator that could be utilized for high-temperature scanning tunneling microscopy to avoid vibrational noise from a graphite substrate. It should be noted that there is no shear phonon in 1LG or 1L-MoS₂. The ρ values for the under-layered heterostructures for the former system are close to 0. This property makes MRS an extraordinarily sensitive tool for analysing the surface and interfacial states of crystals. For composite lattice vibrators (Fig. 4b), the MRS signal of a homojunction (that is, a folded-10LG sample) shows exactly the same MRS features as 20LG, which means that all atomic layers in a homojunction vibrate as a whole, essentially as a result of having the same interlayer force constant. Unlike the folded-MLG, which presents emergent $v_{N,N-1}$ modes enhanced by a twist-induced van Hove singularity resonance in optical Raman scattering³², folded-MLG in MRS exhibits the overall scattering properties of 2MLG with all $v_{2N,2N-1}$ modes that do not depend on the twist angle. On the other hand, in a 3L-MoS₂/4L-WSe₂ vibrator, besides the characteristic MRS features (v_i) of 3L-MoS₂, we observed clear MRS features (v_j) of the underlying 4L-WSe₂ (Supplementary Fig. 12). This intriguing feature is in accordance with the propagation behaviour of a mechanical wave, which suggests the capability of MRS for remote detection of hidden interfaces.

In this Article we have presented an MRS technique that is a particularly powerful tool for the global characterization of mechanical effects in interfacial interactions. We have unambiguously demonstrated that the quantum features of phonon vibrators can be passed on to the plasmonic metal. This kind of quantum-state transfer between nanoscale objects will open up various unforeseen applications in quantum mechanics and quantum optics^{39,40}. Furthermore, because of its physical nature, MRS is a general process that can couple with a range of mechanical and acoustic vibrators, as well as phonons in condensed matter that have net translation displacements. Finally, MRS is also a universal and convenient approach for mechanical modulation of the wavelength of light with a vibrator, providing ultimate-accuracy wavelength control with broadband compatibility.

Online content

Any methods, additional references, Nature Portfolio reporting summaries, source data, extended data, supplementary information, acknowledgements, peer review information; details of author contributions and competing interests; and statements of data and code availability are available at <https://doi.org/10.1038/s41566-023-01181-5>.

References

- Hunt, B. et al. Massive Dirac fermions and Hofstadter butterfly in a van der Waals heterostructure. *Science* **340**, 1427–1430 (2013).
- Xu, W. G. et al. Correlated fluorescence blinking in two-dimensional semiconductor heterostructures. *Nature* **541**, 62–67 (2017).
- Huang, B. et al. Layer-dependent ferromagnetism in a van der Waals crystal down to the monolayer limit. *Nature* **546**, 270–273 (2017).
- Cao, Y. et al. Unconventional superconductivity in magic-angle graphene superlattices. *Nature* **556**, 43–50 (2018).
- Burch, K. S., Mandrus, D. & Park, J. G. Magnetism in two-dimensional van der Waals materials. *Nature* **563**, 47–52 (2018).
- Tran, K. et al. Evidence for moiré excitons in van der Waals heterostructures. *Nature* **567**, 71–75 (2019).
- Kim, S. E. et al. Extremely anisotropic van der Waals thermal conductors. *Nature* **597**, 660–665 (2021).
- Geim, A. K. & Grigorieva, I. V. Van der Waals heterostructures. *Nature* **499**, 419–425 (2013).
- Hong, X. P. et al. Ultrafast charge transfer in atomically thin MoS₂/WS₂ heterostructures. *Nat. Nanotechnol.* **9**, 682–686 (2014).
- Tan, P. H. et al. The shear mode of multilayer graphene. *Nat. Mater.* **11**, 294–300 (2012).
- Quan, J. M. et al. Phonon renormalization in reconstructed MoS₂ moiré superlattices. *Nat. Mater.* **20**, 1100–1105 (2021).
- Zhang, K. et al. Enhancement of van der Waals interlayer coupling through polar Janus MoSSe. *J. Am. Chem. Soc.* **142**, 17499–17507 (2020).
- Luckyanova, M. N. et al. Coherent phonon heat conduction in superlattices. *Science* **338**, 936–939 (2012).
- Long, D. A. & Long, D. *The Raman Effect: a Unified Treatment of the Theory of Raman Scattering by Molecules* Vol. 8 (Wiley, 2002).
- Madeo, J. et al. Directly visualizing the momentum-forbidden dark excitons and their dynamics in atomically thin semiconductors. *Science* **370**, 1199–1203 (2020).
- Wu, B. et al. Visible-light photoexcited electron dynamics of scandium endohedral metallofullerenes: the cage symmetry and substituent effects. *J. Am. Chem. Soc.* **137**, 8769–8774 (2015).
- Roelli, P., Galland, C., Piro, N. & Kippenberg, T. J. Molecular cavity optomechanics as a theory of plasmon-enhanced Raman scattering. *Nat. Nanotechnol.* **11**, 164–169 (2016).
- Chen, W., Roelli, P., Hu, H., Verlekar, S. & Galland, C. Continuous-wave frequency upconversion with a molecular optomechanical nanocavity. *Science* **374**, 1264–1267 (2021).
- Xomalis, A., Zheng, X., Chikkaraddy, R., Koczor-Benda, Z. & Baumberg, J. J. Detecting mid-infrared light by molecular frequency upconversion with dual-wavelength hybrid nanoantennas. *Science* **374**, 1268–1271 (2021).
- Benz, F. et al. Single-molecule optomechanics in ‘picocavities’. *Science* **354**, 726–729 (2016).
- Nie, S. & Emory, S. Probing single molecules and single nanoparticles by surface-enhanced Raman scattering. *Science* **275**, 1102–1106 (1997).
- Kneipp, K., Wang, Y., Kneipp, H., Perelman, L. T. & Feld, M. S. Single molecule detection using surface-enhanced Raman scattering (SERS). *Phys. Rev. Lett.* **78**, 1667–1670 (1997).
- Li, J. F. et al. Shell-isolated nanoparticle-enhanced Raman spectroscopy. *Nature* **464**, 392–395 (2010).
- Zhang, R., Dong, Y., Jiang, Z. C. & Chen, S. C. Chemical mapping of a single molecule by plasmon-enhanced Raman scattering. *Nature* **498**, 82–86 (2013).
- Joonhee et al. Visualizing vibrational normal modes of a single molecule with atomically confined light. *Nature* **568**, 78–92 (2019).
- Xu, J. Y. et al. Determining structural and chemical heterogeneities of surface species at the single-bond limit. *Science* **371**, 818–822 (2021).
- Ding, S. Y., Yi, J., Li, J. F., Ren, B. & Tian, Z. Q. Nanostructure-based plasmon-enhanced Raman spectroscopy for surface analysis of materials. *Nat. Rev. Mater.* **1**, 16021 (2016).
- Gonzalez-Rubio, G. et al. Femtosecond laser reshaping yields gold nanorods with ultranarrow surface plasmon resonances. *Science* **358**, 640–644 (2017).
- Duan, S., Rinkevicius, Z., Tian, G. J. & Luo, Y. Optomagnetic effect induced by magnetized nanocavity plasmon. *J. Am. Chem. Soc.* **141**, 13795–13798 (2019).
- Sharma, B., Frontiera, R. R., Henry, A. I., Ringe, E. & Van Duyne, R. P. SERS: materials, applications and the future. *Mater. Today* **15**, 16–25 (2012).
- Butt, H. J. & Jaschke, M. Calculation of thermal noise in atomic-force microscopy. *Nanotechnology* **6**, 1–7 (1995).
- Cong, C. X. & Yu, T. Enhanced ultra-low-frequency interlayer shear modes in folded graphene layers. *Nat. Commun.* **5**, 4709 (2014).
- Meyer, J. C. et al. On the roughness of single- and bi-layer graphene membranes. *Solid State Commun.* **143**, 101–109 (2007).

34. Wang, G. R. et al. Bending of multilayer van der Waals materials. *Phys. Rev. Lett.* **123**, 116101 (2019).
35. Meyer, J. C. et al. The structure of suspended graphene sheets. *Nature* **446**, 60–63 (2007).
36. Salvetat, J. P. et al. Elastic and shear moduli of single-walled carbon nanotube ropes. *Phys. Rev. Lett.* **82**, 944–947 (1999).
37. van Baren, J. et al. Stacking-dependent interlayer phonons in 3R and 2H MoS₂. *2D Mater.* **6**, 025022 (2019).
38. Lee, C., Wei, X. D., Kysar, J. W. & Hone, J. Measurement of the elastic properties and intrinsic strength of monolayer graphene. *Science* **321**, 385–388 (2008).
39. Riedinger, R. et al. Non-classical correlations between single photons and phonons from a mechanical oscillator. *Nature* **530**, 313–316 (2016).
40. Yu, H. Y., Liu, G. B., Tang, J. J., Xu, X. D. & Yao, W. Moiré excitons: from programmable quantum emitter arrays to spin-orbit-coupled artificial lattices. *Sci. Adv.* **3**, e1701696 (2017).

Publisher's note Springer Nature remains neutral with regard to jurisdictional claims in published maps and institutional affiliations.

Springer Nature or its licensor (e.g. a society or other partner) holds exclusive rights to this article under a publishing agreement with the author(s) or other rightsholder(s); author self-archiving of the accepted manuscript version of this article is solely governed by the terms of such publishing agreement and applicable law.

© The Author(s), under exclusive licence to Springer Nature Limited 2023

Methods

Sample preparation

Kish graphite (Covalent Materials Corp.), MoS₂ and WSe₂ crystals (HQ graphene), and h-BN crystal (2D semiconductors) were used for the preparation of mono-component lattice vibrators on SiO₂/Si substrates via the mechanical exfoliation method⁴¹. Multi-component lattice vibrators were fabricated via the dry-process aligned-transfer method with the aid of polydimethylsiloxane films (Gel-Pak)². Undoped silicon wafers were chosen for a minimum scattering background in the low-frequency region. Plasmonic-active Ag/Au nanoisland films were directly prepared on top of lattice vibrators by the vacuum thermal-evaporation method (8-nm Au or 5-nm Ag films were deposited at a rate of 0.3–0.5 Å s⁻¹). According to our investigations, the as-prepared plasmonic metal films or nanoisland films, after an additional annealing procedure in a reductive atmosphere (Ar:H₂ = 1:1 at 200 °C for 120 min), are both MRS-active under the present measurement conditions⁴². Fabrication of the size-controlled nanodisk arrays was realized by electron-beam lithography. Poly methyl methacrylate (PMMA, MicroChem) resist was spin-coated on the sample (2,000 r.p.m., 60 s) and then baked at 180 °C for 1.5 min. The nanodisk patterns were written directly on the PMMA resist on top of graphite using a scanning electron microscope equipped with an electron-beam lithography module (TESCAN MIRA3). The exposed chips were immersed in an MIBK:IPA (3:1) mixed solution for 30 s to finalize development, then a 30-nm Ag film was deposited without any adhesion layer by vacuum thermal evaporation. Subsequently, the chips were immersed in acetone to remove the PMMA template. The samples with Ag nanodisks were rinsed with isopropyl alcohol (IPA) and then dried with a nitrogen-gas flow before spectroscopic measurements.

Micro-area reflectance spectroscopy

We used a confocal micro-Raman spectrometer (Horiba–LabRAM HR Evolution) with a 600-lines-per-mm grating for the micro-area reflectance measurements. The system covers a spectral range of 300–1,700 nm and has a spatial resolution below 4 μm. Using a halogen lamp as the white-light source, the reflectance spectra of a sample (*R*) and SiO₂/Si substrate (*R*₀) were collected, then the final micro-area reflectance spectra ($\Delta R/R_0$) were obtained according to $(R - R_0)/R_0$ (Supplementary Fig. 7).

Ultralow-frequency Raman spectroscopy

We used the same confocal micro-Raman spectrometer to implement measurements of the ultralow-frequency Raman spectra. For both 532-nm (2.33 eV) and 633-nm (1.96 eV) excitation, we used multiple BraggGrate notch filters (BNFs, each with an FWHM of ~5–10 cm⁻¹) to remove plasma lines and to cut off the Rayleigh scattering background. The optical path was optimized with L-cystine standard samples, providing a low-frequency measurement limit of ~4 cm⁻¹. A 1,800-lines-per-mm grating was used to provide a spectral resolution of ~0.31 cm⁻¹. The $\tilde{z}(xy)$ z-polarizer configuration was used to suppress the background signal⁴⁰. The laser power could be tuned by a series of neutral density filters (Thorlabs).

All spectral measurements were conducted with a ×100 objective lens (Olympus, numerical aperture 0.90) under ambient conditions, if not otherwise noted. The in situ temperature-dependent MRS measurements were conducted in a liquid-nitrogen continuous-flow cryostat (Cryo Industry of American), and a ×100 objective with correction

collar (Leica, numerical aperture 0.85) was used for calibration of the spherical aberration after passing an optical window. The spectrometer was calibrated before each set of measurements using a standard neon lamp. All spectra are reported without smoothing.

Data availability

The datasets generated during and/or analysed during the current study are available from the corresponding author on reasonable request. Source data are provided with this paper.

References

- Novoselov, K. S. et al. Two-dimensional atomic crystals. *Proc. Natl Acad. Sci. USA* **102**, 10451–10453 (2005).
- Xu, W. G. et al. Graphene-veiled gold substrate for surface-enhanced Raman spectroscopy. *Adv. Mater.* **25**, 928–933 (2013).

Acknowledgements

This work was supported by the National Natural Science Foundation of China (22173044, 21873048 and 22073017), the Natural Science Foundation of Jiangsu Province (BK20220121), the National Key R&D Program of China (2020YFA0406104), the Fundamental Research Funds for the Central Universities in China (021014380177), the Frontiers Science Center for Critical Earth Material Cycling of Nanjing University (DLTD2110), 'Innovation & Entrepreneurship Talents Plan' of Jiangsu Province and the Innovation Program for Quantum Science and Technology (2021ZD0303301, 2021ZD0303303 and 2021ZD0303305). Z.J. acknowledges funding support from the CAS Interdisciplinary Innovation Team and the National Natural Science Foundation of China (12074371).

Author contributions

W.X. and S.F. conceived the initial idea. W.X., Y.L., S.D. and S.F. designed the experiments. S.F. fabricated the samples and performed the spectroscopy measurement experiments with help from L.L., H.L., B.J., C.L., N.W. and L.Z., and Y.Y., S.C. and X. Wen performed finite-difference time-domain simulations. S.D., J.Z., X. Wang, D.X., Y.L. and W.X. contributed to theoretical analyses. S.F. collected and organized all experimental data. S.F., S.D., X. Wang, H.L., Y.L. and W.X. co-wrote the manuscript, with input from all authors.

Competing interests

The authors declare no competing interests.

Additional information

Supplementary information The online version contains supplementary material available at <https://doi.org/10.1038/s41566-023-01181-5>.

Correspondence and requests for materials should be addressed to Daiqian Xie, Yi Luo or Weigao Xu.

Peer review information *Nature Photonics* thanks the anonymous reviewers for their contribution to the peer review of this work.

Reprints and permissions information is available at www.nature.com/reprints.